Monthly Notices of the ROYAL ASTRONOMICAL SOCIETY

MNRAS **436,** 2625–2638 (2013) doi:10.1093/mnras/stt1767
Advance Access publication 2013 October 15

Broad-band monitoring tracing the evolution of the jet and disc in the black hole candidate X-ray binary MAXI J1659−152

A. J. van der Horst,[1★] P. A. Curran,[2] J. C. A. Miller-Jones,[2] J. D. Linford,[3] J. Gorosabel,[4,5,6] D. M. Russell,[7,8] A. de Ugarte Postigo,[4,9] A. A. Lundgren,[10] G. B. Taylor,[3] D. Maitra,[11] S. Guziy,[12] T. M. Belloni,[13] C. Kouveliotou,[14] P. G. Jonker,[15,16,17] A. Kamble,[16] Z. Paragi,[18] J. Homan,[19] E. Kuulkers,[20] J. Granot,[21] D. Altamirano,[1] M. M. Buxton,[22] A. Castro-Tirado,[4] R. P. Fender,[23] M. A. Garrett,[24,25] N. Gehrels,[26] D. H. Hartmann,[27] J. A. Kennea,[28] H. A. Krimm,[26,29] V. Mangano,[30] E. Ramirez-Ruiz,[31] P. Romano,[30] R. A. M. J. Wijers,[1] R. Wijnands[1] and Y. J. Yang[1]

[1]*Astronomical Institute, University of Amsterdam, Science Park 904, NL-1098 XH Amsterdam, the Netherlands*
[2]*International Centre for Radio Astronomy Research – Curtin University, GPO Box U1987, Perth, WA 6845, Australia*
[3]*Department of Physics and Astronomy, University of New Mexico, MSC074220, Albuquerque, NM 87131-0001, USA*
[4]*Instituto de Astrofísica de Andalucía (IAA-CSIC), Glorieta de la Astronomía s/n, E-18008 Granada, Spain*
[5]*Unidad Asociada Grupo Ciencia Planetarias UPV/EHU-IAA/CSIC, Departamento de Física Aplicada I, E.T.S. Ingeniería, Universidad del País Vasco UPV/EHU, Alameda de Urquijo s/n, E-48013 Bilbao, Spain*
[6]*Ikerbasque, Basque Foundation for Science, Alameda de Urquijo 36-5, E-48008 Bilbao, Spain*
[7]*Instituto de Astrofísica de Canarias (IAC), Vía Láctea s/n, E-38205 La Laguna, S/C de Tenerife, Spain*
[8]*Departamento de Astrofísica, Universidad de La Laguna, E-38205 La Laguna, S/C de Tenerife, Spain*
[9]*Dark Cosmology Centre, Niels Bohr Institute, Juliane Maries Vej 30, D-2100 Copenhagen Ø, Denmark*
[10]*Joint ALMA Observatory, Alonso de Córdova 3107, Vitacura, Santiago, Chile*
[11]*Department of Astronomy, University of Michigan, 500 Church Street, Ann Arbor, MI 48109, USA*
[12]*Nikolaev National University, Nikolska 24, Nikolaev 54030, Ukraine*
[13]*INAF – Osservatorio Astronomico di Brera, Via E. Bianchi 46, I-23807 Merate (LC), Italy*
[14]*Space Science Office, ZP12, NASA/Marshall Space Flight Center, Huntsville, AL 35812, USA*
[15]*SRON, Netherlands Institute for Space Research, Sorbonnelaan 2, NL-3584 CA Utrecht, the Netherlands*
[16]*Harvard-Smithsonian Center for Astrophysics, 60 Garden Street, Cambridge, MA 02138, USA*
[17]*Department of Astrophysics/IMAPP, Radboud University Nijmegen, PO Box 9010, NL-6500 GL Nijmegen, the Netherlands*
[18]*Joint Institute for VLBI in Europe, Postbus 2, NL-7990 AA Dwingeloo, the Netherlands*
[19]*Massachusetts Institute of Technology, Kavli Institute for Astrophysics and Space Research, Cambridge, MA 02139, USA*
[20]*European Space Astronomy Centre (ESA/ESAC), Science Operations Department, E-28691 Villanuevadela Cañada (Madrid), Spain*
[21]*Department of Natural Sciences, The Open University of Israel, PO Box 808, Ra'anana 43537, Israel*
[22]*Astronomy Department, Yale University, PO Box 208101, New Haven, CT 06520-8101, USA*
[23]*School of Physics and Astronomy, University of Southampton, Southampton, Hampshire SO17 1BJ, UK*
[24]*Netherlands Institute for Radio Astronomy (ASTRON), Postbus 2, NL-7990 AA Dwingeloo, the Netherlands*
[25]*Leiden Observatory, University of Leiden, Postbus 9513, NL-2300 RA Leiden, the Netherlands*
[26]*NASA/Goddard Space Flight Center, 8800 Greenbelt Road, Greenbelt, MD 20771, USA*
[27]*Department of Physics and Astronomy, Clemson University, Clemson, SC 29634-0978, USA*
[28]*Department of Astronomy and Astrophysics, Pennsylvania State University, University Park, PA 16802, USA*
[29]*Universities Space Research Association, 10211 Wincopin Circle, Suite 500, Columbia, MD 21044, USA*
[30]*INAF, Istituto di Astrofysica Spaziale e Fisica Cosmica – Palermo, Via U. La Malfa 153, I-90146 Palermo, Italy*
[31]*Department of Astronomy and Astrophysics, University of California, Santa Cruz, CA 95064, USA*

Accepted 2013 September 16. Received 2013 September 10; in original form 2013 August 20

ABSTRACT

MAXI J1659−152 was discovered on 2010 September 25 as a new X-ray transient, initially identified as a gamma-ray burst, but was later shown to be a new X-ray binary with a black

★ E-mail: a.j.vanderhorst@uva.nl

© 2013 The Authors
Published by Oxford University Press on behalf of the Royal Astronomical Society

Downloaded from http://mnras.oxfordjournals.org/ at NASA Goddard Space Flight Ctr on September 2, 2014

hole as the most likely compact object. Dips in the X-ray light curves have revealed that MAXI J1659−152 is the shortest period black hole candidate identified to date. Here we present the results of a large observing campaign at radio, submillimetre, near-infrared (nIR), optical and ultraviolet (UV) wavelengths. We have combined this very rich data set with the available X-ray observations to compile a broad-band picture of the evolution of this outburst. We have performed broad-band spectral modelling, demonstrating the presence of a spectral break at radio frequencies and a relationship between the radio spectrum and X-ray states. Also, we have determined physical parameters of the accretion disc and put them into context with respect to the other parameters of the binary system. Finally, we have investigated the radio–X-ray and nIR/optical/UV–X-ray correlations up to ∼3 yr after the outburst onset to examine the link between the jet and the accretion disc, and found that there is no significant jet contribution to the nIR emission when the source is in the soft or intermediate X-ray spectral state, consistent with our detection of the jet break at radio frequencies during these states.

Key words: stars: individual: MAXI J1659−152 – X-rays: binaries – X-rays: individual: MAXI J1659–152.

1 INTRODUCTION

Black hole X-ray binaries (BHXBs) are usually discovered as transient sources, with a large outburst in X-rays accompanied by increased emission at ultraviolet (UV), optical, near-infrared (nIR) and radio wavelengths (for a review, see e.g. McClintock & Remillard 2006; Belloni 2010; Fender 2010; Gallo 2010; Gilfanov 2010). These systems spend most of their time in a quiescent state, where the optical/nIR emission is emitted by the companion star or the cool accretion disc. The flux across the electromagnetic spectrum increases by orders of magnitude during outbursts, which are powered by increased accretion on to the black hole and can last weeks to months. The radio emission in these outbursts is ascribed to a relativistic jet, and sometimes these sources are named microquasars by analogy to radio-loud active galactic nuclei (Mirabel et al. 1992).

During an outburst BHXBs go through several canonical X-ray spectral states, following a typical trajectory in the hardness–intensity diagram (HID; e.g. Homan et al. 2001; Homan & Belloni 2005; Belloni 2010). Typically, the source will first become significantly brighter while the spectrum is relatively hard and power-law dominated (hard state), after which the source will become spectrally soft and thermal dominated (soft state); and it eventually dims and evolves back to the hard and then quiescent states. The various spectral states can also be associated with different time variability behaviour and the presence of certain types of quasi-periodic oscillations (QPOs; e.g. Wijnands, Homan & van der Klis 1999; Casella, Belloni & Stella 2005; Motta et al. 2011). There are various classifications in the literature for the different states, based on spectral and timing behaviour. In this paper we follow Homan & Belloni (2005) and Belloni (2010) in identifying the hard-intermediate state (HIMS) and soft-intermediate state (SIMS) in between the hard and soft states (see McClintock & Remillard 2006, for an alternative classification).

The X-ray emission is thought to be produced in the accretion disc and/or a hot corona above the disc, and the UV, optical and nIR emission is also produced in the accretion disc, either intrinsically (e.g. Shakura & Sunyaev 1973) or by reprocessing of X-rays in that same region (e.g. van Paradijs & McClintock 1994). At nIR to optical wavelengths there may also be a contribution from the jet that dominates the radio emission (e.g. Corbel & Fender 2002; Russell et al. 2006). The latter emission is usually described by a flat spectrum and it is bright during the initial hard state. In some models there is also a contribution from the jet at X-ray frequencies (e.g. Markoff & Nowak 2004). During the transition to the soft state the radio emission is quenched, and in some sources discrete ejecta are launched and their radio emission can be spatially resolved (e.g. Fender, Belloni & Gallo 2004).

On 2010 September 25 a new transient was discovered with the Burst Alert Telescope (BAT) onboard the *Swift* satellite, which was initially identified as a gamma-ray burst (GRB) and named GRB 100925A (Mangano et al. 2010). The source was independently detected as a peculiar hard X-ray emitting source by the Gas Slit Camera (GSC) of the Monitor of All-sky X-ray Image (MAXI) instrument onboard the *International Space Station*, and was designated as MAXI J1659−152 (Negoro et al. 2010). Soon after its discovery it was realized that this new transient was not a GRB (Kann 2010; Xu 2010), and observations with the X-shooter spectrograph at the ESO Very Large Telescope (VLT) identified the source as an X-ray binary (de Ugarte Postigo et al. 2010a; Kaur et al. 2012). The nature of the source was confirmed by the *Rossi X-ray Timing Explorer* (*RXTE*), classifying it as a black hole candidate (Kalamkar et al. 2010) based on the identification of its low-frequency QPOs. MAXI J1659−152 evolved through the X-ray hardness–intensity diagram in a manner characteristic of low-mass X-ray binaries, and the presence of type B and type C QPOs, and the way in which they evolve during the outburst, have provided evidence for the black hole nature of the compact object (Kalamkar et al. 2011; Muñoz-Darias et al. 2011).

Further observations at X-ray and soft gamma-ray energies with *Swift* (Kennea et al. 2010), *INTEGRAL* (Kuulkers et al. 2010), *RXTE* (e.g. Belloni, Muñoz-Darias & Kuulkers 2010a), MAXI and *XMM–Newton* have shown that there are dips in the light curves recurring at a period of 2.414 ± 0.005 h (Kuulkers et al. 2013). These have been interpreted as absorption dips at the orbital period of the system, which makes MAXI J1659−152 the shortest period black hole candidate known to date (Kennea et al. 2011; Kuulkers et al. 2012, 2013). For absorption dips to occur, the inclination angle of the accretion disc with respect to the line of sight is relatively well constrained at ∼65°–80°. This allows for an estimate of the binary orbital separation, and mass and radius of the donor star. The binary system appears to be compact (orbital separation of $>1.33\,R_{\odot}$) and the companion is suggested to be an M5 or M2 dwarf star (Kong 2012; Kuulkers et al. 2013).

Downloaded from http://mnras.oxfordjournals.org/ at NASA Goddard Space Flight Ctr on September 2, 2014

After the source discovery we initiated a broad-band follow-up campaign. Besides many of the aforementioned observations at X-ray and soft gamma-ray energies, we observed the source in various UV, optical and nIR bands, and at submillimetre and several radio frequencies. A varying optical source was detected with the *Swift* Ultraviolet and Optical Telescope (UVOT; Marshall 2010), and in the *R*-band with BOOTES-2 and IAC80 (Jelinek et al. 2010), while optical variability on minute time-scales was found with the Faulkes Telescope (Russell et al. 2010a). At submillimetre wavelengths MAXI J1659−152 was detected with the Atacama Pathfinder Experiment (APEX; de Ugarte Postigo et al. 2010b), and at radio frequencies with the Westerbork Synthesis Radio Telescope (WSRT; van der Horst et al. 2010a). We followed the evolution of the outburst during various transitions at X-ray (Belloni, Motta & Muñoz-Darias 2010b; Muñoz-Darias et al. 2010; Shaposhnikov & Yamaoka 2010) and radio (Paragi et al. 2010; van der Horst et al. 2010c) wavelengths.

Here we present the results of our observing campaign across the electromagnetic spectrum, focusing on the broad-band modelling of several epochs for which we have well covered spectral energy distributions (SEDs) including observations at several radio frequencies, and on correlations between the different spectral regimes. In Section 2 we describe all our broad-band observations and data analysis, and in Section 3 we present the resulting light curves. Our broad-band spectral modelling is detailed in Section 4, while we discuss the radio–X-ray and nIR/optical/UV–X-ray correlations in the context of other BHXBs in Section 5. We summarize and conclude in Section 6. All uncertainties in measured quantities and modelling parameters are quoted at the 1σ confidence level.

2 OBSERVATIONS AND DATA ANALYSIS

2.1 Radio

We observed MAXI J1659−152 at radio and submillimetre frequencies ranging from 610 MHz to 345 GHz, using the WSRT, Karl G. Jansky Very Large Array (VLA), Australia Telescope Compact Array (ATCA) and Giant Metrewave Radio Telescope (GMRT). The results of our radio campaign are given in Table 1, and the upper panel of Fig. 1 shows the light curves for four of our radio observing frequencies to illustrate the broad-band radio evolution of the outburst.

Very Long Baseline Interferometry (VLBI) observations with the European VLBI Network (EVN) and Very Long Baseline Array (VLBA) are presented in Paragi et al. (2013). Resulting fluxes of these observations are not included here, since the source is resolved in those, but we have included the WSRT synthesis-array fluxes from the two EVN observations.

2.1.1 Very Large Array

We used the VLA to observe MAXI J1659−152 over multiple epochs at 5, 8, 22 and 43 GHz, starting on 2010 September 28 (MJD 55467) and ending on 2010 December 24 (MJD 55554), as detailed in Table 1. The VLA was in the DnC configuration (maximum baseline of 1.9 km) for the observations from September 28 to October 2, and in the C configuration (maximum baseline of 3.4 km) from October 7 through the end of our observations. We used the new WIDAR correlator with two subbands and 64 channels per subband covering a bandwidth of 128 MHz (i.e. 256 MHz in total). We selected 3C 286 for our absolute flux calibrator and used two nearby calibration sources, J1707−1415 and J1658−0739, to apply complex gain calibration. For polarization measurements, we used OQ 208 as our leakage calibrator.

We performed all of our calibration and reduction in the Astronomical Image Processing System (AIPS; Wells 1985), using standard procedures for radio frequency interference (RFI) excision, spectral channel selection and calibration. For estimating the systematic uncertainties in our measured flux densities, we went by the guidelines outlined in the VLA Calibrator Manual. We added in quadrature systematic uncertainties of 3 (4.9 and 8.5 GHz) and 5 per cent (22 and 43 GHz) of the measured flux densities. As with any new instrument, we experienced some 'teething trouble' with the VLA. Our first observing run produced little useful data. We only managed to get time on MAXI J1659−152 but had no time on 3C 286 for flux calibration and only one scan per band on J1658−0739. We used measurements of J1658−0739 from our second observing run to bootstrap fluxes from the first run. We also missed 3C 286 at 8.5 GHz during our observing run on 2010 October 11 (MJD 55480) and had to bootstrap the flux calibration using J1707−1415. These problems resulted in significantly higher uncertainties for these two observations.

We determined the degree of polarization in our 5 and 8 GHz observations in the first two weeks of the outburst. We did not detect any significant polarization in our measurements, with 3σ upper limits varying from 1 to 5 per cent in the first three epochs, and tens of per cent in the fourth epoch. At later epochs the polarization limits are less constraining due to the reduced brightness of the source.

2.1.2 Westerbork Synthesis Radio Telescope

We performed observations of MAXI J1659−152 with the WSRT at 1.4, 2.3 and 4.9 GHz, using the multifrequency front ends (Tan 1991) in combination with the IVC+DZB back end in continuum mode, with a bandwidth of 8 × 20 MHz at all observing frequencies. Complex gain calibration was performed using the calibrator 3C 286 for all observations. The observations were analysed using the Multichannel Image Reconstruction Image Analysis and Display (MIRIAD; Sault, Teuben & Wright 1995) software package, except for the WSRT data that were obtained during VLBI observations, which were analysed with AIPS. The flux uncertainties were determined with the MIRIAD task IMFIT, to which the rms noise in the image around MAXI J1659−152 was added in quadrature.

With the initial discovery of the radio counterpart of MAXI J1659−152 we also reported a high degree of linear polarization in the source (van der Horst et al. 2010a). However, careful re-analysis of this first epoch, and also analysis of the other WSRT epochs at 4.9 GHz, does not show any significant polarization, consistent with the non-detections of polarized emission with the VLA.

2.1.3 Australia Telescope Compact Array

MAXI J1659−152 was observed with the ATCA for 4.5 h on 2010 September 28 (MJD 55467). We used the Compact Array Broadband Backend (CABB; Wilson et al. 2011) to observe simultaneously in two separate frequency bands, centred at 5.5 and 9.0 GHz. Each frequency band comprised 2048 channels, each of width 1 MHz, for a total observing bandwidth of 2048 MHz. The array was in its H75 configuration, with five closely spaced antennas within 82 m, and a more distant sixth antenna 4.4 km away.

Downloaded from http://mnras.oxfordjournals.org/ at NASA Goddard Space Flight Ctr on September 2, 2014

Table 1. Radio and submillimetre observations of MAXI J1659−152, with ΔT the number of days after MJD 55464.0 (the source discovery date). WSRT* indicates WSRT observations taken as part of EVN e-VLBI runs (Paragi et al. 2013). Upper limits are given at the 3σ level.

Epoch (MJD)	ΔT (d)	Observatory	0.61 GHz (mJy)	1.4 GHz (mJy)	2.3 GHz (mJy)	4.9 GHz (mJy)	8.5 GHz (mJy)	22 GHz (mJy)	43 GHz (mJy)	345 GHz (mJy)
55464.96–55465.08	1.02	APEX	–	–	–	–	–	–	–	15.8 ± 3.0
55465.59–55465.82	1.70	WSRT	–	–	–	5.39 ± 0.05	–	–	–	–
55467.05–55467.13	3.09	VLA	–	–	–	10.30 ± 1.03	–	10.00 ± 1.05	–	–
55467.17–55467.34	3.25	ATCA	–	–	–	9.76 ± 0.06	11.29 ± 0.06	–	–	–
55467.51–55467.83	3.67	WSRT	–	6.95 ± 0.14	6.68 ± 0.08	–	–	–	–	–
55468.05–55468.13	4.09	VLA	–	–	–	9.88 ± 0.30	10.03 ± 0.31	11.81 ± 0.71	11.19 ± 0.59	–
55469.63–55469.76	5.69	WSRT*	–	–	–	9.77 ± 0.10	–	–	–	–
55470.06–55470.15	6.10	VLA	–	–	–	10.29 ± 0.32	9.74 ± 0.30	8.84 ± 0.49	4.84 ± 0.35	–
55471.50–55471.82	7.66	WSRT	–	9.02 ± 0.16	9.40 ± 0.08	–	–	–	–	–
55471.98–55472.06	8.02	VLA	–	–	–	9.23 ± 0.28	7.55 ± 0.42	7.88 ± 0.42	3.74 ± 0.40	–
55473.58–55473.75	9.66	WSRT*	–	–	–	3.65 ± 0.09	–	–	–	–
55473.97–55474.06	10.01	APEX	–	–	–	–	–	–	–	10.5 ± 3.2
55475.95–55476.07	12.01	APEX	–	–	–	–	–	–	–	<6.0
55476.48–55476.80	12.64	WSRT	–	1.15 ± 0.10	1.26 ± 0.06	–	–	–	–	–
55476.96–55477.04	13.00	VLA	–	–	–	0.63 ± 0.03	0.59 ± 0.03	0.41 ± 0.07	<0.10	–
55479.90–55480.05	15.97	APEX	–	–	–	–	–	–	–	<6.3
55480.97–55481.01	16.99	VLA	–	–	–	0.59 ± 0.03	0.65 ± 0.06	–	–	–
55482.98–55483.03	19.00	VLA	–	–	–	0.95 ± 0.04	0.88 ± 0.04	–	–	–
55484.46–55484.78	20.62	WSRT	–	2.23 ± 0.12	–	2.03 ± 0.06	–	–	–	–
55488.37–55488.49	24.43	GMRT	<0.42	–	–	–	–	–	–	–
55488.45–55488.77	24.61	WSRT	–	<0.27	<0.23	–	–	–	–	–
55488.99–55489.03	25.01	VLA	–	–	–	0.23 ± 0.03	<0.069	<0.25	–	–
55494.31–55494.52	30.42	GMRT	<0.15	–	–	–	–	–	–	–
55499.90–55499.94	35.92	VLA	–	–	–	<0.072	<0.066	–	–	–
55554.64–55554.69	90.66	VLA	–	–	–	0.081 ± 0.016	–	–	–	–

Data were converted to FITS format using the MIRIAD software package, and then read into the Common Astronomy Software Applications (CASA) package for data editing, calibration and imaging. We used PKS 1934−638 as the primary calibrator, and J1733−1304 as the secondary calibrator. One of the central antennas was shadowed during observations of the primary calibrator, so had to be flagged. After editing out bad data and performing external gain calibration, we made a naturally weighted image of the field containing MAXI J1659−152, using the multifrequency synthesis algorithm in CASA to accurately deconvolve sources with non-zero spectral slopes. Owing to the large hole in the *uv* coverage arising from the isolation of the sixth antenna, we only used data from the inner antennas during the imaging process, providing an angular resolution of 65 and 42 arcsec at 5.5 and 9.0 GHz, respectively. However, a comparison with higher resolution VLA data shows that there were no bright confusing sources within these large beams, so the relatively poor angular resolution should not affect our photometry.

A second observation was made on 2010 October 1 (MJD 55470), with a central frequency of 2.1 GHz. Owing to the RFI affecting the majority of the observing bandwidth, and to the short duration of the observation (1.5 h), we were unable to use these data to place any accurate constraints on the brightness of the target source.

2.1.4 Giant Metrewave Radio Telescope

GMRT observed the field of MAXI J1659−152 on 2010 October 19 and 25 (MJD 55488 and 55494, respectively) at an observing frequency of 610 MHz. Radio sources 3C 286 and J1626−298 were used as flux and phase calibrators, respectively. The flux calibrator was observed for about 15 min at the start of the target observations. The phase calibrator and the field of MAXI J1659−152 were then observed alternately for 6 and 45 min. The analysis of the observations was carried out using AIPS, and resulted in non-detections at this frequency.

2.2 Submillimetre

Continuum observations at 870 μm (i.e. 345 GHz) were carried out using the Large APEX Bolometer Camera (LABOCA; Siringo et al. 2009) installed on the Atacama Pathfinder Experiment (APEX; Lundgren et al. 2010). Data were acquired at four epochs under good weather conditions (zenith opacity values ranged from 0.17 to 0.43 at 870 μm). Observations were performed using the wobbler on-off mode and data were reduced using the bolometer array (BoA) analysis software. The total on-source integration time of the four epochs was 8.6 h. The telescope pointing was checked every hour, finding an rms pointing accuracy of 2.1 arcsec. Calibration was performed using observations of the primary calibrators Mars, Uranus and Neptune, as well as the secondary calibrators G10.62, IRAS 16293 and G5.89. The absolute flux calibration uncertainty is estimated to be 11 per cent.

2.3 Near-infrared, optical and ultraviolet

The nIR (*J*- and *H*-band) observations were performed using the 1.3-m telescope [previously the Two Micron All-Sky Survey (2MASS) southern telescope] at the Cerro Tololo Inter-American Observatory (CTIO), which is currently operated by the Small and Moderate Aperture Research Telescope System (SMARTS) consortium (Subasavage et al. 2010). We observed MAXI J1659−152 with an almost daily cadence between 2010 September 29 (MJD 55468) and October 14 (MJD 55483). The data were recorded by a Rockwell HgCdTe Astronomical Wide Area Infrared Imager. Multiple dithered frames were taken and then flat-fielded, sky subtracted,

Downloaded from http://mnras.oxfordjournals.org/ at NASA Goddard Space Flight Ctr on September 2, 2014

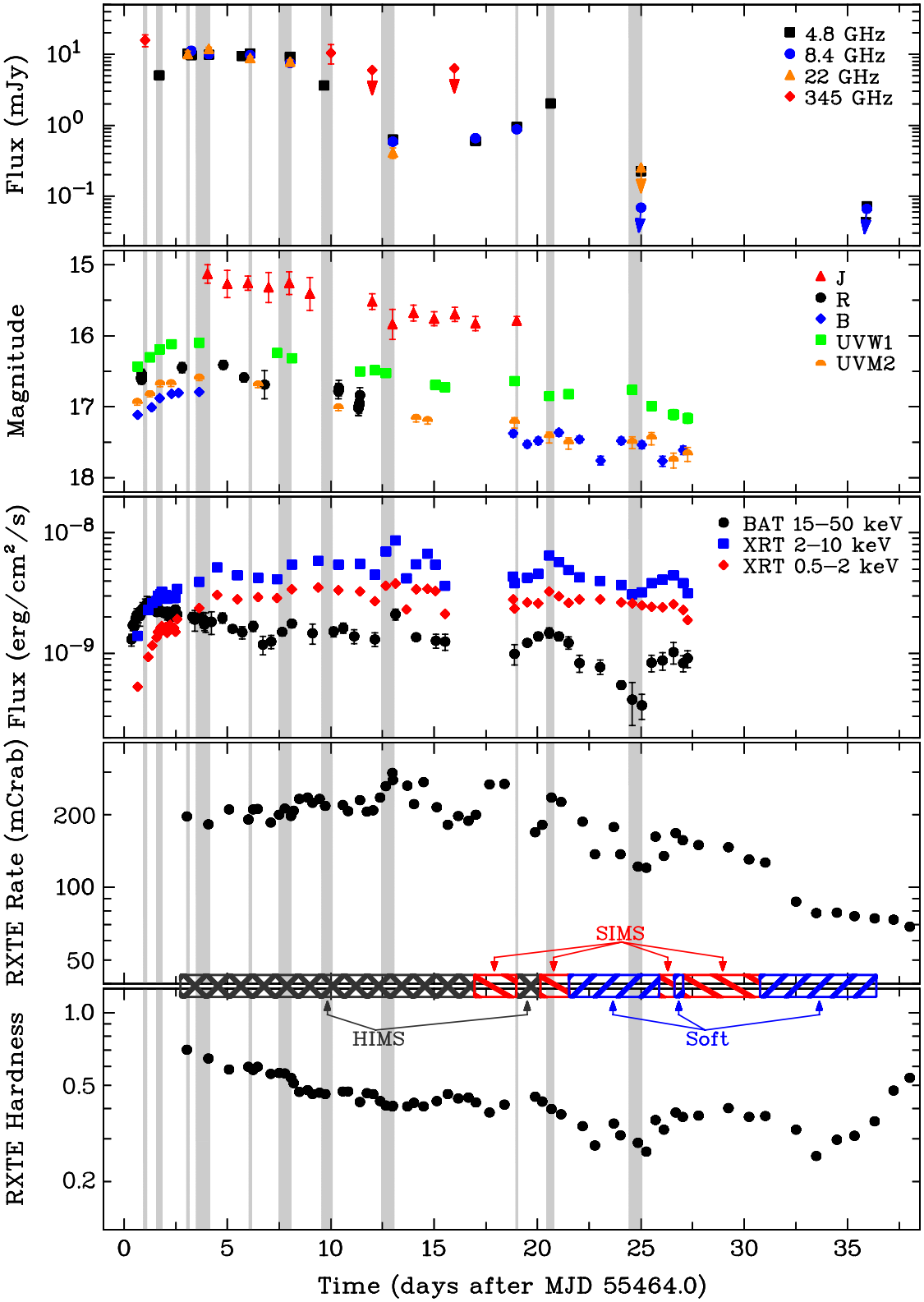

Figure 1. Light curves at various radio and submillimetre wavelengths (top panel), in nIR/optical/UV bands (second panel from the top), from *Swift*/BAT and *Swift*/XRT (middle panel) and from *RXTE* (2–15 keV; second panel from the bottom); and the *RXTE* hardness ratio (6–15 keV/2–6 keV; bottom panel). The vertical grey bars indicate the epochs for which we performed broad-band SED modelling. The times when the source was in the various X-ray states (HIMS, SIMS or soft state) are also indicated (following Muñoz-Darias et al. 2011). Note that the source was in the hard state in the first hours after the outburst onset, but the exact transition from hard state to HIMS is unknown due to the lack of *RXTE* observations.

Downloaded from http://mnras.oxfordjournals.org/ at NASA Goddard Space Flight Ctr on September 2, 2014

aligned and average combined using an in-house IRAF script. We used two nearby 2MASS stars in the field of MAXI J1659−152 as references. The average magnitudes of these comparison stars were used as a basis for differential photometry with respect to MAXI J1659−152. Additional late-time deep observations in the *J* band were carried out with the 3.5-m Centro Astronómico Hispano Alemán (CAHA) telescope on 2013 July 24 (MJD 56497) with a total integration time of 38 min, resulting in a significant detection of 21.05 ± 0.17 mag, ∼3 yr after the outburst onset.

Optical observations were carried out with the IAC80, 1.23-m CAHA, 2.2-m CAHA, 2.0-m Liverpool, BOOTES-2/Telma and BOOTES-3/Yock-Allen telescopes. The IAC80 telescope is a 0.82-m aperture facility, and the observations were done with the CAMELOT camera which is based on a 2k × 2k E2V CCD providing a pixel scale of 0.3 arcsec pixel^{-1}. The 1.23-m CAHA, BOOTES-2/Telma and BOOTES-3/Yock-Allen facilities are Ritchey–Chretien telescopes. The 1.23-m CAHA data were acquired with a 2048 × 2048 SITE#2b CCD which yields a pixel scale of 0.5 arcsec pixel^{-1}. Both BOOTES stations are equipped with identical cameras, an Andor iXon-889+ electron multiplying CCD of 1024 × 1024 pixels, with a pixel scale 0.6 arcsec pixel^{-1} (see Castro-Tirado et al. 1999, for more details on the BOOTES network of telescopes). The IAC80 and the 1.23-m observations were carried out using standard Johnson/Cousins filters (Fukugita, Shimasaku & Ichikawa 1995), while the images of both BOOTES stations were acquired using Sloan filters (Fukugita et al. 1996).

The 2.0-m Liverpool Telescope (LT) observations were made in the SDSS i' band with RATCam, which yields a pixel scale of 0.135 arcsec pixel^{-1} based on a 2048 × 2048 pixel EEV CCD42-40. Additional $g'r'i'z'$-band observations were carried out with the 2.2-m Calar Alto telescope equipped with BUSCA. BUSCA is a multichannel camera which allows simultaneous direct imaging in four optical bands using three CCD485 Lockheed Martin plus one CCD485 backside thinned CCD (in the *uv* channel). The BUSCA observations were done in 2 × 2 binning and 1k × 1k windowing mode, yielding a pixel scale of 0.35 arcsec pixel^{-1} and a field of view of 6 × 6 arcmin^2.

The reduction of all the optical data was performed using standard procedures implemented in IRAF. Calibration of the Sloan data was carried out transforming the Johnson magnitudes of 22 field stars based on Jordi, Grebel & Ammon (2006). The source looks relatively isolated in optical images: there are no entries in either the 2MASS (Skrutskie et al. 1995) or USNO-B1.0 (Monet et al. 2003) catalogues consistent with the position of MAXI J1659−152. Furthermore, observations with the Canada–France–Hawaii Telescope at ∼18 months after the start of the X-ray outburst result in a quiescent *r*-band magnitude of ∼23.6 (Kong 2012). We hence assume that the flux at the time of our analysis was dominated by the transient emission of MAXI J1659−152.

Data from the *Swift* UV/Optical Telescope were downloaded from the High Energy Astrophysics Science Archive Research Center (HEASARC) archive and pre-processed at the *Swift* Data Center (see Breeveld et al. 2010), and required only minimum user processing with the *Swift* FTOOLS as follows. The image data from each filter, from each observation sequence, were summed using UVOTIMSUM. Photometry of the source in individual sequences was derived via UVOTMAGHIST, using an extraction region of radius 5 arcsec. XSPEC compatible spectral files were created with that same region using UVOT2PHA. The obtained magnitudes are based on the UVOT photometric system (Poole et al. 2008).

In Table 2 we give the results of our ground-based optical follow-up campaign and the *Swift*/UVOT observations.

Table 2. UV, optical and nIR observations. The complete Table is available in online version of the article.

Epoch (MJD)	Telescope	Filter	Magnitude
55468.050	SMARTS	*H*	14.70 ± 0.13
55468.995	SMARTS	*H*	14.85 ± 0.12
55469.999	SMARTS	*H*	14.88 ± 0.21
55470.990	SMARTS	*H*	14.90 ± 0.18
–	–	–	–

2.4 X-rays

The outburst of MAXI J1659−152 was observed by several X-ray satellites and instruments. In this paper we focus on the *Swift*, *RXTE* and MAXI observations.

The light curves and spectra of the *Swift* X-Ray Telescope (XRT) were obtained from the XRT online tool, which offers science grade products (Evans et al. 2009). *Swift* Burst Alert Telescope (BAT) data were downloaded from the HEASARC archive and initially processed with the FTOOL BATSURVEY, which applies standard corrections. Eight-channel spectra and response files were extracted and the standard spectral systematic error correction applied with BATPHASYSERR. All X-ray spectra were binned to have ≥20 counts per bin (with GRPPHA) so that errors would be approximately Gaussian and hence χ^2 statistics would be valid.

We analysed all 65 observations of MAXI J1659−152 in the *RXTE* archive. For each observation we extracted a background and dead-time corrected energy spectrum from the Proportional Counter Array (PCA) standard mode, using only data from Proportional Counter Unit (PCU) 2 of the PCA, as it is the best calibrated and the only one which is always active. We used the standard HEASOFT *RXTE* software to create energy spectra. From these spectra, we extracted background-corrected count rates in the PCA channel bands A = 0–35 (2–15 keV; total band), B = 0–13 (2–6 keV; soft band) and C = 14–35 (6–15 keV; hard band). The *RXTE* rate A, converted to Crab units for PCU 2 (conversion factor of 1 Crab = 2284 counts sec^{-1}), was used as *RXTE* rate in Figs 1 and 6, while the hardness was defined as the ratio C/B.

The daily count rate (2–20 keV) and hardness (4–10 keV/2–4 keV) as measured by the MAXI instrument have been taken from the MAXI website.[1]

3 BROAD-BAND LIGHT CURVES

Fig. 1 shows a broad-band overview of the light curves that we obtained in our follow-up campaign of MAXI J1659−152. In this figure we show the light curves at various radio frequencies, nIR, optical and UV bands, and X-ray and soft gamma-ray energies, from the observations presented in Section 2. We do not show light curves in all observing bands to avoid cluttering, but these selected observing bands illustrate the broad-band evolution of the MAXI J1659−152 outburst well. For comparison we also show the *RXTE* count rate light curve and hardness evolution, and indicate the times when the source is in the various X-ray states (HIMS, SIMS or soft state), following the identification of these spectral states for MAXI J1659−152 by Muñoz-Darias et al. (2011). We note that the source was only in the hard state during the first hours after outburst onset, before the start of the *RXTE* observations. Because there are

[1] http://maxi.riken.jp

Downloaded from http://mnras.oxfordjournals.org/ at NASA Goddard Space Flight Ctr on September 2, 2014

no *RXTE* observations during the first two days, we cannot identify the exact time of the transition between the hard state and the HIMS.

It can be seen in Fig. 1 that the source evolved in different ways in the various parts of the electromagnetic spectrum. In almost all wavebands we witnessed the rise of the source brightness, except for our APEX submillimetre observations which do not have the required temporal sampling, and the nIR observations which started around the peak of the outburst at those wavelengths. The observed trends in the optical, UV and X-ray light curves have been described in Kennea et al. (2011), with a correlated fast rise and slow decay at these frequencies, while the late-time X-ray behaviour has been discussed in Homan et al. (2013). At radio frequencies the source was already fairly bright at 1.7 d after the start of the outburst (MJD 55464.0), and reached maximum brightness around day 3. During the following 5 d the radio brightness was constant, after which there was a sudden large decrease of the radio emission (van der Horst et al. 2010c). This radio flux drop was followed several days later by a transition from the hard-intermediate to the soft-intermediate state at X-ray energies (Belloni et al. 2010b), and the radio flux started rising again after that. Other BHXBs have shown that at the transition to the SIMS, fast radio jets in the form of optically thin, discrete ejecta may emerge. This has, however, not been seen for MAXI J1659−152 (Paragi et al. 2013). After the second rise, the flux dropped significantly again at day 20 after the beginning of the outburst, and subsequently it was only detected at very low flux levels (Miller-Jones et al. 2011; Jonker et al. 2012).

4 BROAD-BAND SPECTRAL MODELLING

Given our rich broad-band data set we performed broad-band SED modelling. The grey vertical bands in Fig. 1 indicate the 11 epochs for which this was done. We made our selection of the epochs based on the times for which we had radio data available. In the X-ray bands we used *Swift*/XRT and *Swift*/BAT data.

The broad-band radio-to-X-ray spectra were fit within XSPEC (12.7.1), using χ^2 statistics and accounting for interstellar extinction and absorption, which were modelled by REDDEN and TBABS, respectively. The observed radio and optical flux densities F_ν at frequency ν were converted to flux per filter $F_{\rm filter}$ in units of photons cm^{-2} s^{-1}. This was done via $F_{\rm filter} = 1509.18896 F_\nu\ (\Delta\lambda/\lambda)$, where λ and $\Delta\lambda$ are the effective wavelength and width of respective filters. This flux was then used to produce XSPEC compatible files for spectral fitting, using the FTOOL FLX2XSP.

At all epochs the data were well fit by a phenomenological broken power law at radio frequencies, and by a physically motivated irradiated disc model (DISKIR) at optical/UV and X-ray frequencies (Malzac, Dumont & Mouchet 2005; Gierliński, Done & Page 2008, 2009). In the latter model the X-ray emission consists of thermal emission from the accretion disc and a hard tail caused by Comptonization of soft seed photons in a hot plasma of energetic electrons. The Comptonized emission in turn illuminates the disc, of which a large fraction gets reflected, but also a significant fraction of the photons are reprocessed and add to the disc emission. The parameters of this model are the unilluminated disc temperature, $kT_{\rm disc}$, the power-law photon index Γ of the Compton tail, the ratio of luminosity in the Compton tail to that in the unilluminated, disc, $L_{\rm C}/L_{\rm disc}$, the fraction of bolometric flux which is thermalized in the outer disc, $F_{\rm out}$, the log of the ratio of outer to inner disc radius, $r_{\rm out}$, and a normalization, Norm, dependent on the apparent inner disc radius. We note that it has been shown that spectra can be fit by an irradiated disc model even in the hard state (e.g. Miller, Homan & Miniutti 2006; Rykoff et al. 2007).

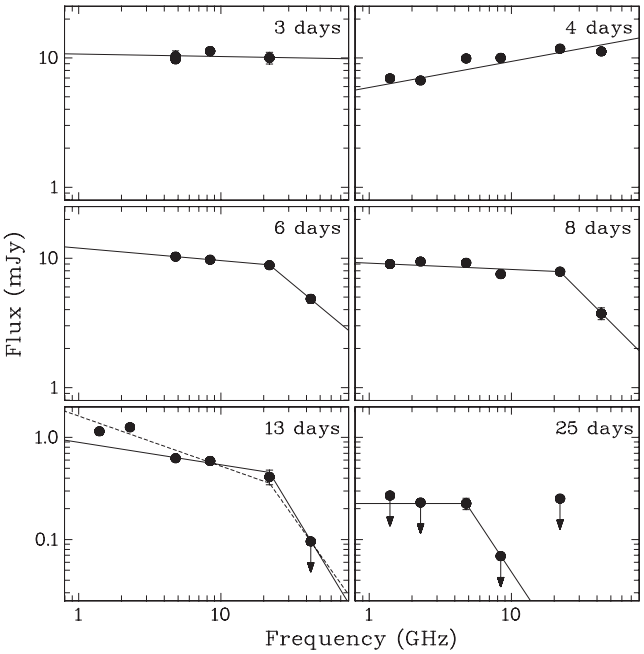

Figure 2. Radio spectra of MAXI J1659−152 for the six epochs for which we have at least three observing bands. The lines indicate the (broken) power-law fits to the radio spectra. The solid and dashed lines for the spectrum at day 13 show the fits with and without including the low-frequency WSRT data below 3 GHz.

The χ^2_ν of the fits presented in the next section ranges from 1.1 to 2.0 for $\sim 10^3$ degrees of freedom, which are relatively high but given the disparity of the data (combination of many different instruments, epochs and bands) we deemed those acceptable. Furthermore, any variations from the model show no underlying structure, only noise-like variations.

4.1 Modelling results

In our modelling the radio emission and the nIR to X-ray emission appear to be due to separate components. Fig. 2 shows the radio spectra for six of our 11 epochs for which we have at least three radio bands. The behaviour of the radio SEDs seems more complicated than a single flat or slightly inverted spectrum across all radio bands (i.e. a spectral index ∼0). We performed single and/or broken power-law fits to the radio SEDs for the epochs indicated in Fig. 1 except for the first two epochs in which there was only one observing frequency. From Fig. 2 it can be seen that there are epochs where a single power law is not sufficient to describe the spectrum, which is the case for four out of the nine epochs we fit. For the latter epochs we show both spectral indices in Fig. 3, while for the other five epochs we only show a single spectral index. In the broken power-law fits we fixed the break at 22 GHz for the SEDs at 6, 8 and 13 d after MJD 55464.0, while at 25 d it was fixed at 4.9 GHz. In the former three epochs these break frequencies were fixed because the spectrum is consistent with a single power law up to 22 GHz and there is only one data point at 43 GHz to constrain the break, which makes the parameters of a free broken power-law fit hard to constrain. In fact, the break could be at any frequency in between 22 and 43 GHz and thus the high-frequency spectral indices can be steeper that the ones plotted in Fig. 3. At day 25 there is only one detection at 4.9 GHz, hence the lower limit on the low-frequency spectral index and the upper limit on the high-frequency spectral

Downloaded from http://mnras.oxfordjournals.org/ at NASA Goddard Space Flight Ctr on September 2, 2014

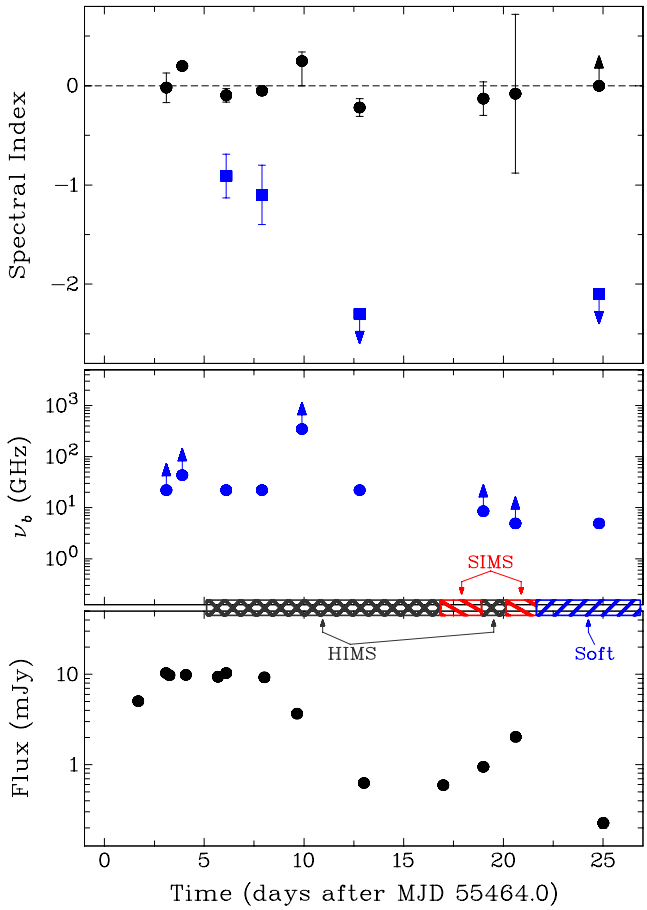

Figure 3. Evolution of parameters from the broken power-law fits to the radio SEDs indicated in Fig. 1 except for the first two epochs. The top panel shows the spectral index, with the black circles indicating the low-frequency power-law slopes, and the blue squares the high frequencies in those epochs that are best described by a broken power law. The middle panel shows the evolution of the spectral break for all epochs, including those for which we can only put upper or lower limits. In the lower panel the 4.9 GHz light curve and the X-ray spectral states are displayed for comparison purposes.

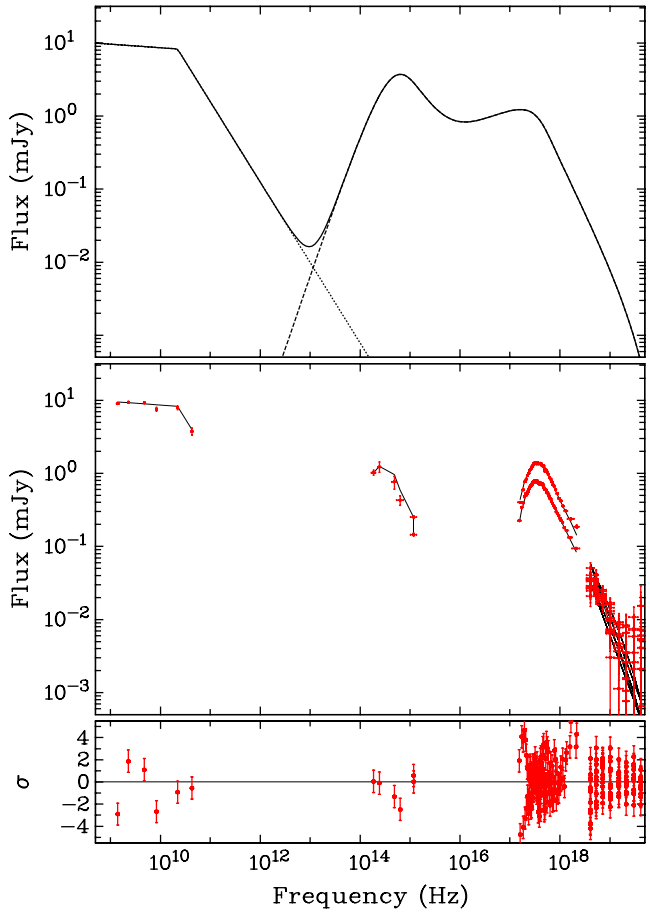

Figure 4. Example model plots for the broad-band SED at day 8 after the outburst onset. The top panel shows the spectrum of the best-fitting model for this particular epoch, with the dotted line showing the broken power-law fit to the radio data, the dashed line the irradiated disc model fit and the solid line the total spectrum. The middle panel shows the fit of the unfolded spectrum, with the data in red symbols and the best-fitting model in black lines. In the bottom panel we show the deviations from the best-fitting model.

index. We would like to point out, however, that the observations are not strictly simultaneous, so the 4.9 GHz detection could be a short flare with a time-scale of hours. For those epochs where a break is not required at radio frequencies, we show lower limits on the break frequency in Fig. 3. In our broad-band radio-to-X-ray fits we placed those breaks arbitrarily at 10^{-5} keV ($\approx 2.4 \times 10^{12}$ Hz), with a steep cut-off.

An example fit to one of the epochs and the broad-band model used here are shown in Fig. 4. $E(B-V)$ displays no significant variability with an average of 0.595 ± 0.008, consistent with the Galactic value of $E(B-V) = 0.599$ (Schlegel, Finkbeiner & Davis 1998). This is significantly larger than the value of $E(B-V) \simeq 0.35$ derived by Kaur et al. (2012). The measured values of interstellar absorption are consistent with being constant with an average of $N_{\rm H} = (0.319 \pm 0.009) \times 10^{22}$ cm^{-2}. This value is greater than the expected Galactic absorption of $N_{\rm H} = 0.17 \times 10^{22}$ cm^{-2} (Kalberla et al. 2005) but less than that obtained by Kennea et al. (2011). It should be noted, however, that Kennea et al. (2011) fit a different model and only to the X-ray data, while we include nIR/optical/UV data which add additional constraints to the thermal emission.

Fig. 5 shows the evolution of the well-constrained parameters of the irradiated disc model. Although the fit parameter values we

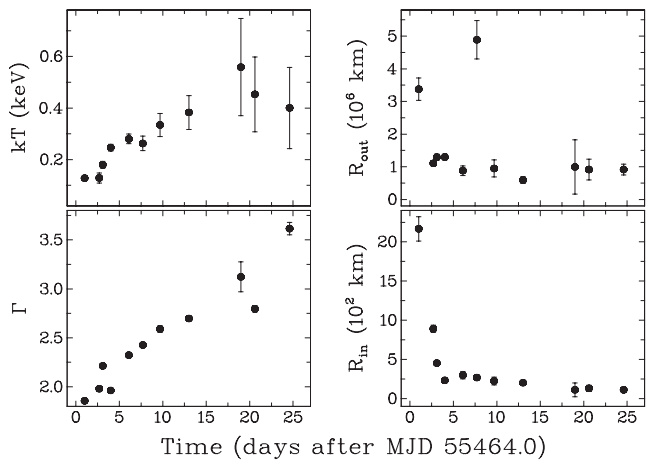

Figure 5. Evolution of the disc temperature (top left), photon index of the Compton tail (bottom left), outer disc radius (top right) and inner disc radius (bottom right). These parameters are based on spectral fits to the broad-band SEDs indicated in Fig. 1, using the irradiated disc model.

Downloaded from http://mnras.oxfordjournals.org/ at NASA Goddard Space Flight Ctr on September 2, 2014

obtain are slightly different than the ones from Kennea et al. (2011) and Yamaoka et al. (2012), the trends in their evolution are similar. The disc temperature, $kT_{\rm disc}$, rises from an initial temperature of 0.13 keV to a relatively stable value of ∼0.3 keV, while the photon index of the tail rises from an initial value of ∼2.0 to a peak of ∼3.6. As the disc temperature rises, the contribution that the Compton tail makes to the disc luminosity, $L_{\rm C}/L_{\rm disc}$, decreases, although this is poorly constrained on many epochs, and at late times is consistent with zero. Likewise, the fraction of bolometric flux which is thermalized in the outer disc, $F_{\rm out}$, decreases although this is also poorly constrained. Since $L_{\rm C}/L_{\rm disc}$ and $F_{\rm out}$ are poorly constrained, we have not plotted them in Fig. 5. The ratio of outer to inner disc radius, $r_{\rm out}$, increases with time which is due to the fact that the inner disc radius is decreasing. Instead of displaying $r_{\rm out}$ and Norm, we show the physical inner radius $R_{\rm in}$ and outer radius $R_{\rm out}$ in Fig. 5. The physical radius $R_{\rm in}$ is related to the apparent radius $r_{\rm in}$ of our fit by $R_{\rm in} \approx 1.19 r_{\rm in}$ (see e.g. Soria 2007). We have determined $r_{\rm in}$ at all the epochs from the fit values of Norm, assuming a source distance of 6 kpc (see Section 5) and an inclination of 70°. $R_{\rm out}$ was derived from $R_{\rm in}$ and the ratio $r_{\rm out}$. In the next section, we will discuss further the trends in the fitted parameters.

4.2 Implications of spectral modelling

4.2.1 Radio SEDs and spectral breaks

In this paper we present several epochs with broad-band radio SEDs. To help place our SED epochs in the overall context of the behaviour of the outburst, we indicate them on the HIDs of both the *RXTE* and MAXI data (Fig. 6). In this figure we have indicated the X-ray observation epochs for which we performed broad-band SED modelling with (quasi-) simultaneous radio data. MAXI J1659−152 was already in the HIMS when the *RXTE* observations started, but from the MAXI HID we can deduce that the source was transitioning from the hard state to the HIMS during the first radio observations, 1–2 d after the outburst onset. Our first radio SED with good broad-band coverage is at ∼3 d after the onset of the X-ray outburst. The radio spectral index α, where $F_\nu \propto \nu^\alpha$, is flat or inverted during the first 10 d over more than an order of magnitude in observing frequency, namely from 1.4 to 22 GHz, as one would expect from a synchrotron emitting, partially self-absorbed jet (Fender 2001) and in full agreement with the observed VLBI structure (see Paragi et al. 2013 and the references therein). The spectrum is not constant over that time-span though, with an inverted spectrum at day 4 with $\alpha = 0.20 \pm 0.02$, while it is flat at other epochs (see Fig. 3). More striking is the sharp spectral break between 22 and 43 GHz that we find on days 6 and 8. After ∼10 d the radio flux drops significantly, but the spectrum is inverted even up to the submillimetre bands.

At day 13 the spectrum appears more complicated, with a sharp spectral break above 22 GHz, and a best-fitting spectral index of $\alpha = -0.49 \pm 0.07$ at lower frequencies. We note, however, that the 1.4 and 2.3 GHz WSRT data were taken roughly 8 h prior to the higher frequency VLA data used to construct the spectrum shown in Fig. 2, and since the source was undergoing a rapid decay, may have overestimated the true low-frequency emission at the time of the VLA observations. Furthermore, any variations from a compact, partially self-absorbed jet will be detected later at lower frequencies, since the lower frequency emission comes from further downstream in the jets. Thus, for a rapidly decaying compact jet, we might expect the lowest frequency emission to be slightly overestimated, relative to the power law seen at higher frequencies. Combined, these two effects could explain the deviation of the low-frequency spectrum on day ∼13 from a pure power law. To mitigate against this effect, we refitted the radio spectrum using only the VLA data between 4.9 and 22 GHz, to give a low-frequency spectral index of $\alpha = -0.22 \pm 0.09$, with a break to $\alpha < -2.3$ above 22 GHz.

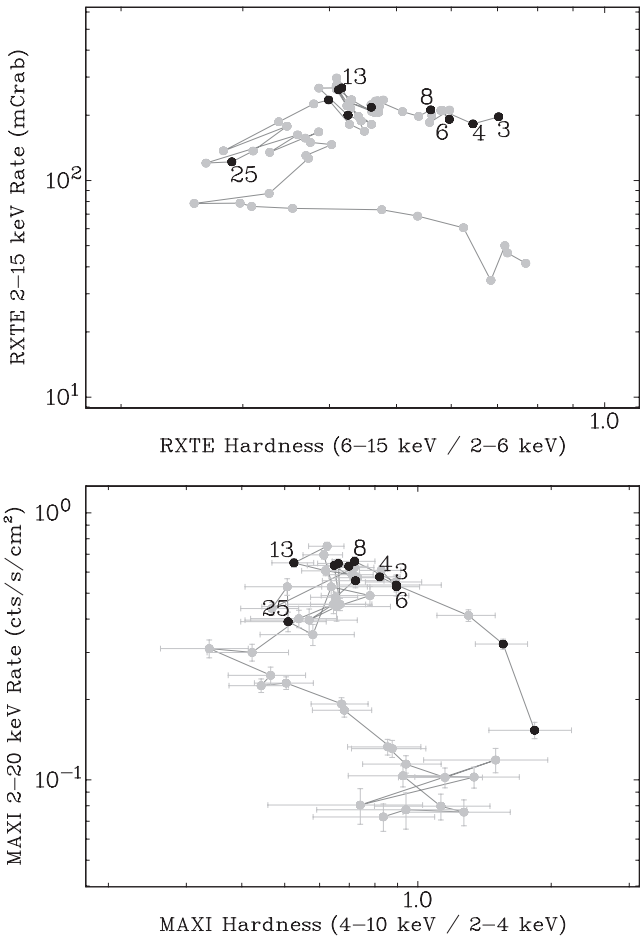

Figure 6. Hardness–intensity diagram for the *RXTE* (top) and MAXI (bottom; up to MJD 55515) data. The black dots indicate the epochs of X-ray observations for which we have (quasi-) simultaneous radio data. We have indicated the epochs on days 3, 4, 6, 8, 13 and 25 from the radio spectra shown in Fig. 2. Note that *RXTE* was not observing MAXI J1659−152 from the outburst onset, hence there is one less black dot in the top panel compared to the bottom panel.

When the radio flux increases again and the source moves into the SIMS, the spectrum remains flat, but we do not have the spectral coverage at high radio frequencies to check for a spectral break. The radio measurements at day 25 are also consistent with being flat or inverted, but then with a sharp break in between 4.9 and 8.5 GHz.

From the radio light curves in Fig. 1 and the spectral index evolution in Fig. 3 it appears that the decrease in the radio emission around day 13 after the outburst onset did not coincide with a significant steepening of the spectrum, as observed in other BHXBs (e.g. Kuulkers et al. 1999; Fender et al. 2004; Miller-Jones et al. 2012). The low-frequency radio emission remained consistent with a partially self-absorbed compact jet throughout the HIMS, with no evidence for ejection events, in agreement with the absence of ejecta in the VLBI images of Paragi et al. (2013).

At higher frequencies, however, the radio spectrum exhibited a high-frequency break above 22 GHz from day ∼6 until at least day

Downloaded from http://mnras.oxfordjournals.org/ at NASA Goddard Space Flight Ctr on September 2, 2014

∼13, and the optically thin spectrum appeared to steepen with time. This spectral break can be interpreted as the transition from optically thick and partially self-absorbed to optically thin synchrotron emission, and has previously been observed in several other BHXBs in hard X-ray states although usually at much higher frequencies (Russell et al. 2013a). Recently, Russell et al. (2013b) have shown that the BHXB MAXI J1836−194 has an inverted spectrum with a break towards a steep spectrum moving from the mid-infrared to lower frequencies as the source softens in the X-ray regime, and then back to higher frequencies as it gets harder again. With sufficiently dense monitoring over a broad radio frequency range one could be able to see the spectral break pass through the radio bands, which may explain what is happening between days 6 and 13 in MAXI J1659−152 (i.e. the inverse of what was seen during the reverse transition in GX339-4 by Corbel et al. 2013a). There appears to be a relatively rapid increase in the break frequency on day 10, shifting up to >345 GHz briefly before dropping back to 22 GHz on day 13. Since this is based on a spectrum consisting of flux density measurements at two frequencies, 4.9 and 345 GHz, this break frequency limit is quite uncertain. An inverted spectrum would shift it to a lower value, e.g. with a spectral index of 0.5 the break is at ∼170 GHz, lower than the limit of 345 GHz but still significantly larger than 22 GHz. Nonetheless, the evolution of the break frequency at that time is fast, but this is not unprecedented: in GX 339−4 the spectral break shifted in the mid-infrared by more than an order of magnitude on time-scales of hours when it was in the hard state (Gandhi et al. 2011). Given that the radio-emitting part of the jet is significantly larger than the infrared-emitting region, strong variability on a time-scale of days in the case of MAXI J1659−152 could be expected. Alternatively, this could be a short-lived flare at submillimetre frequencies. Flares get smoothed out and have reduced amplitude at lower frequencies, which could explain the lack of a flare at 4.9 GHz.

The radio light curve shows an increase in flux between day 17 and 21, while the spectrum remains flat. In Figs 1 and 3 it can been seen that this coincides with a state transition (back and forth between the SIMS and the HIMS), consistent with what has been found for other BHXBs (e.g. Corbel et al. 2013a,b; Russell et al. 2013b). From these observations it seems that the jet started quenching in the HIMS and finished in the SIMS, but then recovered through a second HIMS and peaked in the second SIMS phase, before quenching again after a transition into the soft state. These changes in the radio emission coming from the jet and the X-ray state changes suggest a strong link between the accretion flow and the jet. It also shows that reaching the SIMS is no guarantee of a full transition to a jet ejection event, because there is no major radio flare when the sources moves into the soft state, and no discrete ejecta were detected in the VLBI observations (Paragi et al. 2013). Some other BHXBs in outburst also did not have ejection events, for instance Cyg X−1 (Rushton et al. 2012), but that source did not trace out a canonical track in the HID, while MAXI J1659−152 did (Muñoz-Darias et al. 2011). The soft state in MAXI J1659−152, however, was slightly harder than seen in BHXBs with ejection events, and the minimum fractional variability in the soft state was slightly higher (a minimum of 3 per cent, and rising to 8 per cent when the X-ray emission was softest; Muñoz-Darias et al. 2011). The authors attributed this to the high inclination of the system, but if it was instead intrinsic, the implied difference in the behaviour of the accretion flow could be related to the lack of jet ejection events. Miller-Jones et al. (2012) have shown, however, that the ejection event occurs well before reaching the soft state, at the HIMS/SIMS transition (see also Fender, Homan & Belloni 2009). Since the behaviour of MAXI J1659−152 was relatively standard in the HIMS and SIMS, it seems unlikely that the unusual behaviour in the soft state could be causally related to the lack of ejection events.

4.2.2 Physical constraints from the irradiated disc model

In Fig. 5 we show the evolution of the parameters of the irradiated disc model, in particular the disc temperature, the photon index of the Comptonized tail and the inner and outer radius of the accretion disc. From this figure we can see that the source is getting spectrally softer (steeper photon index), the disc temperature is increasing and the inner radius is decreasing, while the outer radius is fairly constant. The latter is not true for the first and sixth epoch, where we have only few NIR/optical data points to constrain the outer radius reliably. Excluding those epochs, the outer radius has a value of ≈0.9–1.6 × 10^6 km, physically realistic considering the orbital separation (Kuulkers et al. 2013) and consistent with the position of the Lagrangian point >10^6 km. The inner radius of the disc is decreasing in time from ∼890 to ∼110 km, as one would expect in the standard picture of the disc evolution during a BHXB outburst. From the final value of $R_{\rm in}$ (at day 25 after the outburst onset) we can put an upper limit on the black hole mass by assuming that $R_{\rm in}$ is larger than the innermost stable circular orbit, $R_{\rm ISCO} \equiv 6GM/c^2$ km for a non-rotating, Schwarzschild black hole. The resulting black hole mass of MAXI J1659−152 is <12 $M_\odot$, consistent with the mass derived by Yamaoka et al. (2012). We note that these mass estimates would be larger if the black hole were spinning and they should be treated with caution since they are model dependent.

5 RADIO–X-RAY AND OPTICAL–X-RAY CORRELATIONS

5.1 Radio versus X-rays

In Section 4.1 we have discussed the related behaviour between the radio and X-ray regime for MAXI J1659−152, and the implied link between the accretion flow and the jet. We explore this further by investigating the correlation between the radio and X-ray luminosities throughout the outburst. This correlation was originally suggested for GX 339−4 when it was in the hard state (Hannikainen et al. 1998) and described by a power law with index ∼0.7 extending three orders of magnitude in luminosity with a turnover at high X-ray luminosities caused by a quenching of the radio emission in the soft state (Corbel et al. 2003; Gallo, Fender & Pooley 2003). This correlation has not only been found and studied in detail for individual sources (e.g. Corbel, Koerding & Kaaret 2008; Corbel et al. 2013a), but also for the sample of BHXBs as a whole (e.g. Gallo et al. 2003). In recent years a more complex picture has revealed itself, with two distinct tracks in the radio/X-ray luminosity plane (e.g. Coriat et al. 2011; Gallo, Miller & Fender 2012). The second track lies below the first one and has a steeper power-law index of ∼1.4. For a few sources it has been shown that there is a transition from the lower to the upper track at low luminosities (Coriat et al. 2011; Ratti et al. 2012).

Fig. 7 shows the correlation for MAXI J1659−152, and a comparison with other BHXBs in the hard state. Besides the radio observations presented in this paper, we included the late-time data from Jonker et al. (2012). The latter paper focused mainly on the late-time evolution when the source was close to quiescence and also showed the early radio fluxes that had been reported in the

Downloaded from http://mnras.oxfordjournals.org/ at NASA Goddard Space Flight Ctr on September 2, 2014

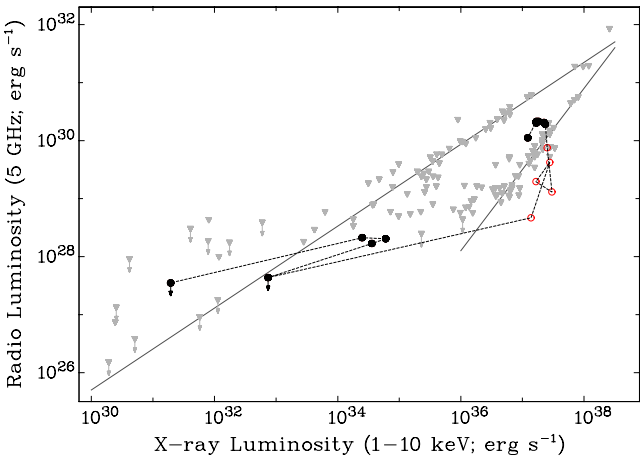

Figure 7. Correlation between the radio and X-ray luminosity during the outburst of MAXI J1659−152, compared to other BHXBs (grey symbols). The grey lines indicate the two tracks in the radio–X-ray correlation with slopes of ∼0.7 and ∼1.4. The MAXI J1659−152 luminosities are calculated for a source distance of 6 kpc. The black solid circles indicate the early times of the outburst when the radio emission in MAXI J1659−152 had not dropped significantly yet (up to day 8 after the outburst onset) and the late times when the source is almost in quiescence (>135 d), while the red open circles indicate the times in between.

literature (Paragi et al. 2010; van der Horst et al. 2010b). To calculate the luminosities we adopted a distance to MAXI J1659−152 of 6 kpc, since the distances estimated in various ways span a range from 4 to 8 kpc (Kennea et al. 2011; Miller-Jones et al. 2011; Kaur et al. 2012; Kuulkers et al. 2013).

As shown by Jonker et al. (2012), MAXI J1659−152 was on the lower track early in the outburst, and once the source had reached quiescent levels, it seemed to transition to the upper track, although we note that the lowest luminosity points have only radio upper limits. With our extensive data set during the early phases of the outburst we show in Fig. 7 that the source gradually evolved off the correlation during the HIMS over the course of several days, as seen before in GX 339−4 (Corbel et al. 2013b) and expected for sources which are not in the hard state. However, the motion in the radio/X-ray plane was not monotonic during this radio quenching, with the radio emission fading and recovering between days 6 and 20, due in part to the repeated transitions between the HIMS and the SIMS.

5.2 Optical versus X-rays

While the radio emission is produced in the jet and the X-ray emission in the accretion disc and/or the corona, the nature of the UV, optical and nIR emission is less unambiguous. Most likely the UV emission is also produced in the accretion disc, either intrinsically or by reprocessing of X-rays, but in the optical and nIR there may also be a contribution from the jet. In Section 4.1 we have modelled the full SED from radio to X-ray frequencies with a combination of a broken power law and a physically motivated irradiated disc model. From these spectral fits we have concluded that a jet contribution at nIR wavelengths is not necessary. This conclusion, however, is model dependent and here we look deeper into this issue by investigating the correlations between the X-ray emission and the nIR, optical and UV emission.

A correlation between the nIR/optical and X-ray luminosity was first found for GX 339−4 in the hard state by Homan et al. (2005),

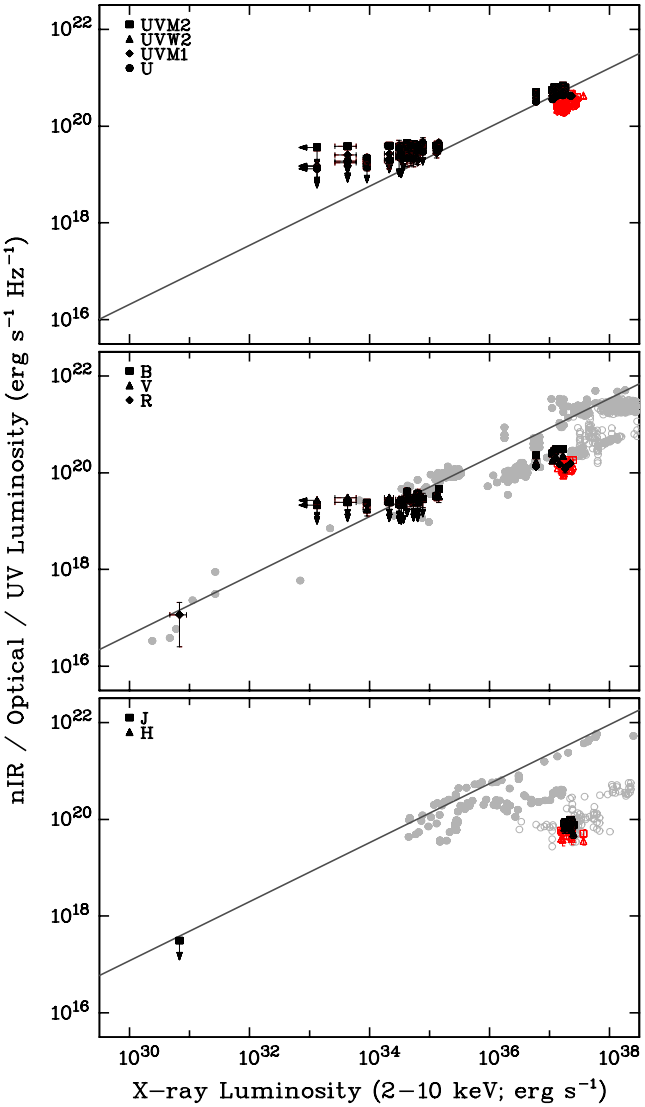

Figure 8. Correlation between the nIR/optical/UV and X-ray luminosity during the outburst of MAXI J1659−152. The MAXI J1659−152 luminosities are calculated for a source distance of 6 kpc. The black solid symbols indicate the early times of the outburst when the radio emission in MAXI J1659−152 had not dropped yet (up to day 8 after the outburst onset) and the late times when the source is almost in or in quiescence (>135 d), while the red open symbols indicate the times in between. The light grey symbols are for other BHXBs during the hard state (solid symbols) and soft state (open symbols) as presented by Russell et al. (2006, 2007). The solid lines show the best-fitting hard state nIR/optical-X-ray correlation from Russell et al. (2006).

with a power-law slope of ∼0.5. Russell et al. (2006) have shown for a large sample of BHXBs in the hard state that there is such a correlation with a power-law slope of ∼0.6 over eight orders of magnitude in X-ray luminosity. A correlation with such a power-law slope can be expected both in the case of X-ray reprocessing (van Paradijs & McClintock 1994) and jet emission at nIR/optical wavelengths. Russell et al. (2006) have also shown that when these sources are in a soft state, the nIR and, in some cases, the optical emission is significantly suppressed. In Fig. 8 we show the correlation between the UV/optical/nIR and X-ray luminosities for MAXI J1659−152. Similar to Fig. 7 we have made a distinction between the early outburst before the radio emission strongly

Downloaded from http://mnras.oxfordjournals.org/ at NASA Goddard Space Flight Ctr on September 2, 2014

decreases (day 8 after the outburst onset; black solid symbols), the second phase of the outburst (red open symbols) and the very late times when the source has reached significantly lower luminosities in the radio, optical and X-rays (black solid symbols). We have also included the optical/nIR detections when the source is in quiescence, using the *r*-band magnitude at ∼1.5 yr after the outburst onset from Kong (2012), the *J*-band magnitude at ∼2.9 yr from this paper, and the quiescent X-ray flux at ∼1.8 yr reported in Homan et al. (2013). From the late-time magnitudes we have subtracted a contribution from the companion star of the black hole. It has been proposed (Kong 2012; Kuulkers et al. 2013) that this is an M2 or M5 dwarf star, which have an absolute *V*-band magnitude of 10 and 11.8, respectively (Kong 2012). We have converted these absolute magnitudes to apparent magnitudes in the *r* and *J* band by correcting for the typical colour of these dwarf stars (Johnson 1965) and galactic extinction, and by adopting a source distance of 6 kpc. The resulting *r*-band magnitude of the companion star is 24.3 (M2) or 25.8 (M5), and in the *J*-band it is 21.1 (M2) or 22.0 (M5). We have corrected the very late time fluxes for these ranges in magnitudes, resulting in the large uncertainties displayed in Fig. 8.

For comparison we plot in Fig. 8 the optical/nIR–X-ray relations for the samples presented in Russell et al. (2006, 2007), although here we show the luminosity divided by observing frequency for optical/nIR frequencies, i.e. the measured flux scaled by the source distance. For the other BHXBs the solid symbols indicate when they are in a hard state, while the open symbols are for the soft state. The top panel of Fig. 8 shows that the UV emission is consistent with the hard state optical–X-ray correlation (Russell et al. 2006) throughout the outburst. In the middle panel it can be seen that MAXI J1659−152 resides in the same region of the correlation as several other hard state BHXBs in the optical, both early in the outburst before the radio emission is quenched and the late times when the source is going towards or is in quiescence. The data corresponding to times after the quenching of the radio emission lay below the correlation of hard state BHXBs, but they are consistent with other sources in the soft state. The bottom panel displays different behaviour at nIR wavelengths: the data are well below the correlation for other hard state sources throughout the main outburst (no late-time nIR observations are available), but consistent with some BHXBs in the soft state. This suggests that at the time of our observations there is no significant contribution of the jet to the nIR emission, which is consistent with our conclusions from the broad-band modelling in Section 4.1. Given the detection of a spectral break at radio frequencies the lack of nIR jet emission is not surprising. We note, however, that our nIR observations started ∼4 d after the outburst onset, and our earliest detection of a break was at ∼6 d, so there is a possibility that the nIR jet emission quenched much earlier than at radio wavelengths. This is consistent with what has been found in other sources, namely that the nIR emission from the jet drops as soon as a source enters the HIMS (e.g. Homan et al. 2005; Coriat et al. 2009; Russell et al. 2010b) while the radio flux quenches later (e.g. Fender et al. 2004), caused by the jet spectral break shifting to lower frequencies.

6 CONCLUSIONS

In this paper we have presented the results of our observing campaign of MAXI J1659−152 across the electromagnetic spectrum, resulting in one of the richest broad-band data sets of a BHXB outburst with observations at radio, submillimetre, nIR, optical, UV and X-ray frequencies, from 1 d up to 3 yr after the outburst onset. We have modelled SEDs from radio to X-ray frequencies at several epochs with a broken power law plus a physical irradiated disc model, and we have presented the radio–X-ray and nIR/optical/UV–X-ray correlations for MAXI J1659−152 in the context of other BHXBs.

We have found changes in the radio brightness and spectrum which are correlated with X-ray state changes, suggesting a link between the radio jet and the accretion flow that is dominating the X-ray emission. We have shown this based on our broad-band SED modelling and by investigating the correlation between radio and X-ray luminosity. During the first weeks after the outburst onset MAXI J1659−152 moved away from the hard state into intermediate X-ray spectral states, based on spectral and timing behaviour at X-ray energies. This was further evidenced by (1) the increasing disc temperature, steepening photon index and decreasing disc inner radius we have found in our SED modelling, (2) the quenching of the radio emission coming from the jet and (3) the deviations from the radio–X-ray and nIR/optical/UV–X-ray correlations of BHXBs in the hard state.

The broad-band radio light curves and spectra support the conclusions from Paragi et al. (2013), based on VLBI observations, that there was no major ejection event. Our radio observations also show the presence of a variable spectral break at radio frequencies during the HIMS and SIMS, significantly lower in frequency than typically found in hard state BHXBs. We have investigated the nIR/optical/UV–X-ray correlations and concluded that there is no significant contribution from the jet at nIR wavelengths, consistent with our broad-band modelling. Taken with the results of Russell et al. (2013b) and Corbel et al. (2013b), this suggests that the spectral break, which lies at infrared frequencies during the hard state, evolves down in frequency during the HIMS and SIMS until it passes through the radio band.

Our findings for MAXI J1659−152 demonstrate that broad-band observations covering several radio and nIR/optical/UV frequencies at a high cadence during BHXB outbursts are important for a better understanding of the jet and disc in these sources. On top of these observations, denser sampling at submillimetre and mid-infrared frequencies are crucial to accurately determine the evolution of the spectral break and further our understanding of the jet physics in these systems.

ACKNOWLEDGEMENTS

We greatly appreciate the support from the VLA, WSRT, APEX, ATCA, GMRT, SMARTS, IAC80, 1.23-m CAHA, BOOTES-2 and BOOTES-3 telescopes in their help with scheduling and obtaining these observations. The National Radio Astronomy Observatory is operated by Associated Universities, Inc., under cooperative agreement with the National Science Foundation. The WSRT is operated by ASTRON (Netherlands Institute for Radio Astronomy) with support from the Netherlands foundation for Scientific Research. APEX is a collaboration between the Max-Plank-Institut für Radioastronomie, the European Southern Observatory and the Onsala Space Observatory. The ATCA is funded by the Commonwealth of Australia for operation as a National Facility managed by CSIRO. The GMRT is operated by the National Center for Radio Astrophysics of the Tata Institute of Fundamental Research. The CTIO 1.3-m telescope is operated by the SMARTS consortium. The Centro Astronómico Hispano Alemán (CAHA) at Calar Alto is operated jointly by the Max-Planck Institut für Astronomie and the Instituto de Astrofísica de Andalucía (CSIC). The Liverpool Telescope is operated on the island of La Palma by Liverpool John Moores University in the Spanish Observatorio del

Downloaded from http://mnras.oxfordjournals.org/ at NASA Goddard Space Flight Ctr on September 2, 2014

Roque de los Muchachos of the Instituto de Astrofisica de Canarias with financial support from the UK Science and Technology Facilities Council. The IAC80 is operated on the island of Tenerife by the IAC in the Spanish Observatorio del Teide. The MAXI/GSC data are provided by RIKEN, JAXA and the MAXI team. This research has made use of data obtained from the High Energy Astrophysics Science Archive Research Center (HEASARC), provided by NASA's Goddard Space Flight Center.

AJvdH and RAMJW acknowledge support from the European Research Council via Advanced Investigator Grant no. 247295. PAC and JCAM-J acknowledge support from the Australian Research Council's *Discovery Projects* funding scheme under grant DP120102393. DMR acknowledges support from a Marie Curie Intra European Fellowship within the Seventh European Community Framework Programme under contract no. IEF 274805. AdUP acknowledges support by the European Commission under the Marie Curie Career Integration Grant programme (FP7-PEOPLE-2012-CIG 322307), and the Dark Cosmology Centre, funded by the DNRF. This work was supported by the Unidad Asociada IAA-CSIC at the group of planetary science of ETSI-UPV/EHU, by the Ikerbasque Foundation for Science, and by Spanish research programs AYA2012-39362-C02-02, AYA2011-24780/ESP, AYA2009-14000-C03-01/ESP and AYA2010-21887-C04-01. TMB acknowledges support from grant PRIN-INAF 2012. RW acknowledges support from the European Research Council via a Starting Grant.

REFERENCES

Belloni T., ed., 2010, Lecture Notes in Physics, Vol. 794, The Jet Paradigm. Springer-Verlag, Berlin
Belloni T. M., Muñoz-Darias T., Kuulkers E., 2010a, Astron. Telegram, 2926
Belloni T. M., Motta S., Muñoz-Darias T., 2010b, Astron. Telegram, 2927
Breeveld A. A. et al., 2010, MNRAS, 406, 1687
Casella P., Belloni T., Stella L., 2005, ApJ, 629, 403
Castro-Tirado A. J. et al., 1999, A&AS, 138, 583
Corbel S., Fender R. P., 2002, ApJ, 573, L35
Corbel S., Nowak M. A., Fender R. P., Tzioumis A. K., Markoff S., 2003, A&A, 400, 1007
Corbel S., Koerding E., Kaaret P., 2008, MNRAS, 389, 1697
Corbel S., Coriat M., Brocksopp C., Tzioumis A. K., Fender R. P., Tomsick J. A., Buxton M. M., Bailyn C. D., 2013a, MNRAS, 428, 2500
Corbel S. et al., 2013b, MNRAS, 431, L107
Coriat M., Corbel S., Buxton M. M., Bailyn C. D., Tomsick J. A., Körding E., Kalemci E., 2009, MNRAS, 400, 123
Coriat M. et al., 2011, MNRAS, 414, 677
de Ugarte Postigo A., Flores H., Wiersema K., Thoene C. C., Fynbo J. P. U., Goldoni P., 2010a, GRB Coordinates Network, Circular Service, 11307, 1
de Ugarte Postigo A., Lundrgren A., Wyrowski F., Thoene C. C., Castro-Tirado A. J., Gorosabel J., Jelinek M., 2010b, GRB Coordinates Network, Circular Service, 11304, 1
Evans P. A. et al., 2009, MNRAS, 397, 1177
Fender R. P., 2001, MNRAS, 322, 31
Fender R., 2010, in Belloni T., ed., Lecture Notes in Physics, Vol. 794, The Jet Paradigm. Springer-Verlag, Berlin, p. 115
Fender R. P., Belloni T. M., Gallo E., 2004, MNRAS, 355, 1105
Fender R. P., Homan J., Belloni T. M., 2009, MNRAS, 396, 1370
Fukugita M., Shimasaku K., Ichikawa T., 1995, PASP, 107, 945
Fukugita M., Ichikawa T., Gunn J. E., Doi M., Shimasaku K., Schneider D. P., 1996, AJ, 111, 1748
Gallo E., 2010, in Belloni T., ed., Lecture Notes in Physics, Vol. 794, The Jet Paradigm. Springer-Verlag, Berlin, p. 85
Gallo E., Fender R. P., Pooley G. G., 2003, MNRAS, 344, 60
Gallo E., Miller B. P., Fender R., 2012, MNRAS, 423, 590
Gandhi P. et al., 2011, ApJ, 740, L13
Gierliński M., Done C., Page K., 2008, MNRAS, 388, 753
Gierliński M., Done C., Page K., 2009, MNRAS, 392, 1106
Gilfanov M., 2010, in Belloni T., ed., Lecture Notes in Physics, Vol. 794, The Jet Paradigm. Springer-Verlag, Berlin, p. 17
Hannikainen D. C., Hunstead R. W., Campbell-Wilson D., Sood R. K., 1998, A&A, 337, 460
Homan J., Belloni T., 2005, Ap&SS, 300, 107
Homan J., Wijnands R., van der Klis M., Belloni T., van Paradijs J., Klein-Wolt M., Fender R., Méndez M., 2001, ApJS, 132, 377
Homan J., Buxton M., Markoff S., Bailyn C. D., Nespoli E., Belloni T., 2005, ApJ, 624, 295
Homan J., Fridriksson J. K., Jonker P. G., Russell D. M., Gallo E., Kuulkers E., Rea N., Altamirano D., 2013, ApJ, 775, 9
Jelinek M. et al., 2010, GRB Coordinates Network, Circular Service, 11301, 1
Johnson H. L., 1965, ApJ, 141, 170
Jonker P. G., Miller-Jones J. C. A., Homan J., Tomsick J., Fender R. P., Kaaret P., Markoff S., Gallo E., 2012, MNRAS, 423, 3308
Jordi K., Grebel E. K., Ammon K., 2006, A&A, 460, 339
Kalamkar M. et al., 2010, Astron. Telegram, 2881
Kalamkar M., Homan J., Altamirano D., van der Klis M., Casella P., Linares M., 2011, ApJ, 731, L2
Kalberla P. M. W., Burton W. B., Hartmann D., Arnal E. M., Bajaja E., Morras R., Pöppel W. G. L., 2005, A&A, 440, 775
Kann D. A., 2010, GRB Coordinates Network, Circular Service, 11299, 1
Kaur R. et al., 2012, ApJ, 746, L23
Kennea J. A., Krimm H., Mangano V., Curran P., Romano P., Evans P., Burrows D. N., 2010, Astron. Telegram, 2877
Kennea J. A. et al., 2011, ApJ, 736, 22
Kong A. K. H., 2012, ApJ, 760, L27
Kuulkers E., Fender R. P., Spencer R. E., Davis R. J., Morison I., 1999, MNRAS, 306, 919
Kuulkers E. et al., 2010, Astron. Telegram, 2912
Kuulkers E. et al., 2012, in Mihara T., Serino M., eds, 4th International MAXI Workshop, IPCR CR-127, The First Year of MAXI: Monitoring Variable X-ray Sources. The Institute of Physical and Chemical Research, Wako, p. 81
Kuulkers E. et al., 2013, A&A, 552, A32
Lundgren A. et al., 2010, Proc. SPIE, 7737, 773708
McClintock J. E., Remillard R. A., 2006, in Lewin W. H. G., van der Klis M., eds, Black Hole Binaries. Cambridge Univ. Press, Cambridge, p. 157
Malzac J., Dumont A. M., Mouchet M., 2005, A&A, 430, 761
Mangano V., Hoversten E. A., Markwardt C. B., Sbarufatti B., Starling R. L. C., Ukwatta T. N., 2010, GRB Coordinates Network, Circular Service, 11296, 1
Markoff S., Nowak M. A., 2004, ApJ, 609, 972
Marshall F. E., 2010, GRB Coordinates Network, Circular Service, 11298, 1
Miller J. M., Homan J., Miniutti G., 2006, ApJ, 652, L113
Miller-Jones J. C. A., Madej O. K., Jonker P. G., Homan J., Ratti E. M., Torres M. A. P., 2011, Astron. Telegram, 3358
Miller-Jones J. C. A. et al., 2012, MNRAS, 421, 468
Mirabel I. F., Rodriguez L. F., Cordier B., Paul J., Lebrun F., 1992, Nat, 358, 215
Monet D. G. et al., 2003, AJ, 125, 984
Motta S., Muñoz-Darias T., Casella P., Belloni T., Homan J., 2011, MNRAS, 418, 2292
Muñoz-Darias T., Stiele H., Belloni T. M., Motta S., 2010, Astron. Telegram, 2999
Muñoz-Darias T., Motta S., Stiele H., Belloni T. M., 2011, MNRAS, 415, 292
Negoro H. et al., 2010, Astron. Telegram, 2873
Paragi Z. et al., 2010, Astron. Telegram, 2906
Paragi Z. et al., 2013, MNRAS, 432, 1319
Poole T. S. et al., 2008, MNRAS, 383, 627

Downloaded from http://mnras.oxfordjournals.org/ at NASA Goddard Space Flight Ctr on September 2, 2014

Ratti E. M. et al., 2012, MNRAS, 423, 2656
Rushton A. et al., 2012, MNRAS, 419, 3194
Russell D. M., Fender R. P., Hynes R. I., Brocksopp C., Homan J., Jonker P. G., Buxton M. M., 2006, MNRAS, 371, 1334
Russell D. M., Maccarone T. J., Körding E. G., Homan J., 2007, MNRAS, 379, 1401
Russell D. M. et al., 2010a, Astron. Telegram, 2884
Russell D. M., Maitra D., Dunn R. J. H., Markoff S., 2010b, MNRAS, 405, 1759
Russell D. M. et al., 2013a, MNRAS, 429, 815
Russell D. M. et al., 2013b, ApJ, 768, L35
Rykoff E. S., Miller J. M., Steeghs D., Torres M. A. P., 2007, ApJ, 666, 1129
Sault R. J., Teuben P. J., Wright M. C. H., 1995, in Shaw R. A., Payne H. E., Hayes J. J. E., eds, ASP Conf. Ser. Vol. 77, Astronomical Data Analysis Software and Systems IV. Astron. Soc. Pac., San Francisco, p. 433
Schlegel D. J., Finkbeiner D. P., Davis M., 1998, ApJ, 500, 525
Shakura N. I., Sunyaev R. A., 1973, A&A, 24, 337
Shaposhnikov N., Yamaoka K., 2010, Astron. Telegram, 2951
Siringo G. et al., 2009, A&A, 497, 945
Skrutskie M. F. et al., 1995, BAAS, 27, 1392
Soria R., 2007, Ap&SS, 311, 213
Subasavage J. P., Bailyn C. D., Smith R. C., Henry T. J., Walter F. M., Buxton M. M., 2010, Proc. SPIE, 7737, 77371C
Tan G. H., 1991, in Cornwell T. J., Perley R. A., eds, ASP Conf. Ser. Vol. 19, IAU Colloq. 131, Radio Interferometry. Theory, Techniques, and Applications. Astron. Soc. Pac., San Francisco, p. 42
van der Horst A. J., Granot J., Paragi Z., Kouveliotou C., Wijers R. A. M. J., Ramirez-Ruiz E., 2010a, GRB Coordinates Network, Circular Service, 11309, 1
van der Horst A. J., Granot J., Paragi Z., Kouveliotou C., Wijers R. A. M. J., Ramirez-Ruiz E., 2010b, Astron. Telegram, 2874
van der Horst A. J. et al., 2010c, Astron. Telegram, 2918
van Paradijs J., McClintock J. E., 1994, A&A, 290, 133
Wells D. C., 1985, in di Gesu V., Scarsi L., Crane P., Friedman J. H., Levialdi S., eds, Data Analysis in Astronomy. Plenum Press, New York, p. 195
Wijnands R., Homan J., van der Klis M., 1999, ApJ, 526, L33
Wilson W. E. et al., 2011, MNRAS, 416, 832
Xu D., 2010, GRB Coordinates Network, Circular Service, 11303, 1
Yamaoka K. et al., 2012, PASJ, 64, 32

SUPPORTING INFORMATION

Additional Supporting Information may be found in the online version of this article:

Table 2. UV, optical and nIR observations (http://mnras.oxfordjournals.org/lookup/suppl/doi:10.1093/mnras/stt1767/-/DC1).

Please note: Oxford University Press is not responsible for the content or functionality of any supporting materials supplied by the authors. Any queries (other than missing material) should be directed to the corresponding author for the article.

This paper has been typeset from a TEX/LATEX file prepared by the author.

Downloaded from http://mnras.oxfordjournals.org/ at NASA Goddard Space Flight Ctr on September 2, 2014